

Supplemental Material

Early onset and late acceleration of rapid exhumation in the Namche Barwa syntaxis, eastern Himalaya

Gwladys Govin^{1†}, Peter van der Beek^{2,3*}, Yani Najman¹, Ian Millar⁴, Lorenzo Gemignani^{5‡}, Pascale Huyghe², Guillaume Dupont-Nivet^{3,6}, Matthias Bernet², Chris Mark^{7§}, Jan Wijbrans⁵

This PDF file includes:

Supplementary Methods:

- Sample Collection and Preparation
- Zircon fission-track (ZFT) dating
- White mica ⁴⁰Ar/³⁹Ar (MAr) dating
- Rutile U-Pb (RUPb) dating
- Decomposition of age populations and inclusion of additional data
- Reasons for obtaining inconsistent minimum-age peaks
- Fitting lag-time trends
- Thermal-kinematic inverse modeling Justification for interpreting rutile U-Pb ages as cooling ages

Figs. S1 to S8

Table S1: Data Synthesis

Table S5: Modeling parameters

Table S6: Inversion Results.

Data Availability Statement

Supplementary References

Other Supplemental material for this manuscript include:

Tables S2 to S4 (csv files):

- Table S2: Zircon fission-track (ZFT) data
- Table S3: White mica ⁴⁰Ar/³⁹Ar (MAr) data
- Table S4: Rutile U-Pb (RUPb) data

SUPPLEMENTARY METHODS

Sample collection and preparation

Ten large sandstone samples were collected from the Siang section, the Remi section and the Sibro outcrop close to Pasighat, eastern Arunachal Pradesh, India (Fig. 1). These sections are described in detail by Govin et al. (2018), who also provide determinations of their depositional ages. The most complete section is the Remi section, composed of Middle and Upper Siwalik sediments with an estimated age range of 1.0 ± 0.2 Ma (sample REM3; Table S1) to 6.1 ± 0.5 Ma (sample REM21, Table S1). Depositional ages for this section were determined by magneto-stratigraphy, aided by detrital apatite fission-track dating to constrain maximum depositional ages (Govin et al., 2018). The Siang section contains Middle Siwalik sediments and is located structurally below the Remi section; maximum depositional ages for this section are constrained by detrital apatite fission-track dating only and are between 7.0 ± 0.3 Ma (sample SG1, Table S1) and 10.0 ± 2.0 Ma (sample SG15, Table S1). The Sibro outcrop exposes slightly tilted (10°) Upper Siwalik deposits; their normal magnetization combined with a saturated luminescence (IRSL-50) signal limits their depositional age to 0.5 ± 0.3 Ma (Govin et al., 2018).

Subsequent to crushing and sieving of samples, heavy minerals were extracted by wet separation on a Haultain superpanner followed by standard heavy liquid and magnetic separation, at the NERC Isotope Geosciences Laboratory (NIGL), Keyworth, UK. Zircon and rutile grains were handpicked, taking special care to select all grain types with respect to morphology, color and grain size, from the corresponding density fraction of the separate. White micas were handpicked from the light fraction, separated with the Haultain superpanner.

Zircon fission-track (ZFT) dating

Zircon grains were mounted in two to four Teflon[®] sheets per sample, polished and etched in a NaOH-KOH solution at 228°C for 36 to 70 hours at ISTerre, Université Grenoble Alpes (France). The multi-mount technique with different etch times allows obtaining countable grains from the whole grain-age spectrum of a sample (Bernet and Garver, 2005). Zircon-grain mounts were covered with muscovite external detectors and irradiated together with IRMM541 dosimeter glasses and Fish Canyon Tuff age standards in the FRMII reactor at the Technical University of Munich (Germany). Following thermal-neutron irradiation, muscovite sheets were etched at 21°C for 18 min in 48% HF. Spontaneous and induced

tracks were counted dry, using an Olympus BH2 optical microscope with 1250× magnification. Between 36 and 105 grains per sample were dated, depending on available sample material and zircon quality with respect to zonation, fractures, inclusions, defects and metamictisation, using a ζ -factor (Hurford and Green, 1983) of 105.8 ± 3.7 . Zircon fission-track data are presented in Table S2 and in Figure S1.

White-mica $^{40}\text{Ar}/^{39}\text{Ar}$ (M_{Ar}) dating

White-mica $^{40}\text{Ar}/^{39}\text{Ar}$ dating by single-grain fusion was performed at the Vrije Universiteit, Amsterdam (The Netherlands). Sample packages, containing >100 mica grains in the size fraction 250-500 μm each, were irradiated along with reference material SA-2 sanidine (Kuiper et al., 2008), for 12 hours in the in-core CLICIT facility of the Oregon State University TRIGA reactor. After irradiation, minerals were unpacked and loaded in Cu sample trays. Single grains were fused with a CO_2 laser; in-sequence measurements of about 50 grains per sample were performed with system blanks measured before, during and after each fourth run. The system blanks were stable and predictable during the runs. Between every 20 runs, air-reference gas measurements were carried out to monitor mass discrimination and system performance. The baseline-corrected beam intensities of the five isotopes of Argon (m/e 40–36) were measured simultaneously on a ThermoFisher Helix MC+ multi-collector noble-gas mass spectrometer. The beam intensities of the ^{40}Ar and ^{39}Ar beams were measured on faraday collectors fitted with a $10^{13} \Omega$ resistor faraday amplifier (Gemignani et al., 2019). The beam intensities of ^{38}Ar and ^{37}Ar were measured on standard compact 257 discrete dynode secondary electron multipliers (SEM) in pulse-counting mode. The beam intensity of ^{36}Ar was measured on a compact discrete dynode SEM fitted with a high-resolution (>1700) collector slit. In this configuration, full resolution between argon and hydrocarbon beams is assured. For off-line data reduction, we used ArArCalc2.5 (Koppers, 2002). The ages are reported with 2σ uncertainties; since small and young grains lead to low sample-beam intensity and are therefore difficult to measure, we applied the following filters to accept or reject results from individual runs: we considered an experiment failed when from the beam intensity data we had to conclude that the grain was not a muscovite but another potassium-poor phyllosilicate, yielding low intensities on ^{39}Ar . In the range 250 - 500 μm , unaltered muscovite grains should have a substantial ^{39}Ar beam; we therefore used a rule-of-thumb intensity criterion of <0.5 V to reject partially altered grains. We also rejected measurements that exceeded a maximum acceptable error interval, set at 100% for grains

with an age <5 Ma; 50% for grains with ages between 5 and 20 Ma, and 20% for grains that yielded ages >20 Ma. White mica $^{40}\text{Ar}/^{39}\text{Ar}$ data are presented in Table S3 and in Figure S2.

Rutile U-Pb (RUPb) dating

Rutiles were mounted in epoxy, polished, and photographed to help identify the analyzed grains. Rutile U-Pb dating was performed using a Nu Instruments AttoM single-collector inductively coupled plasma mass spectrometer (SC-ICP-MS) at NIGL, Keyworth (U.K.). The instrument was tuned to ensure that ThO and UO were less than 0.4% and used in peak-jumping mode with measurement on a MassCom SEM. The analyzed masses in each sweep were: ^{202}Hg , $^{204}\text{Pb}+\text{Hg}$, ^{206}Pb , ^{207}Pb , and ^{235}U . Each data-integration sequence recorded 100 sweeps of the measured masses; dwell times were 400 μs on ^{207}Pb and ^{235}U , and 200 μs on all other masses. ^{238}U is calculated using $^{238}\text{U}/^{235}\text{U} = 137.818$. Laser ablation was performed using a New Wave Research UP193SS laser ablation system with a low-volume cell (Horstwood et al., 2003). Ablation parameters were optimized to suit the Pb and U contents with a frequency of 5 Hz, a fluence of 1.5 to 3.0 J/cm^2 , a 30-second ablation time, and a 30- to 35- μm spot size.

Four rutile reference materials, Sugluk-4, PCA-S207 (Bracciali et al., 2013), R10 and R19 (Luvizotto et al., 2009), were analyzed at regular intervals in order to correct data for instrumental fractionation (some of these analyses failed due to ejection of the relatively small grains from the mount during ablation). The average bias of the $^{207}\text{Pb}/^{206}\text{Pb}$ and $^{206}\text{Pb}/^{238}\text{U}$ ratios from preferred values derived by TIMS analysis were used for normalization. $^{206}\text{Pb}/^{238}\text{U}$ and $^{207}\text{Pb}/^{206}\text{Pb}$ uncertainties were propagated in the manner advocated by Horstwood (2008), utilizing the measurement uncertainty and the reproducibility of the ablation reference material used.

Since rutile is commonly discordant due to relatively high common Pb, model ages were derived by regressing data points through a fixed common-Pb composition of 0.844 ± 0.008 on Tera-Wasserburg plots as described in Bracciali et al. (2013). Analyses with very high common Pb contents are less likely to give meaningful ages using this approach due to the degree of extrapolation involved, and so analyses with $^{207}\text{Pb}/^{206}\text{Pb} > 0.5$ were excluded. In addition, samples with very low Pb concentrations yielded imprecise results, so analyses with < 100 counts of ^{206}Pb were discarded. Rutile U-Pb data are presented in Table S4 and in Figure S3.

Decomposition of age populations and inclusion of additional data

The youngest age populations have been determined for each sample, from the data fraction of accepted ages <30 Ma for ZFT and MAr, and <50 Ma for RUPb, using the minimum-age mixture model (Galbraith, 2005) on a linear density plot in the Density Plotter program (Vermeesch, 2012). As a comparison, automated peak fitting following Vermeesch (2012) was also employed on the full set of accepted ages (Table S1, Figures S1-S3). For practically all samples, the minimum-age peak and the youngest fitted age peak (P1) overlap within uncertainty.

In order to expand the dataset, we included published data for modern river-sand samples as well as samples from a Siwalik section ~50 km downstream (Siji section; Fig. 1) in our analysis. The modern river-sand samples were all collected from the Siang River at Pasighat, they include a composite of samples 301 (Stewart et al., 2008), S (Enkelmann et al., 2011) and LI10-03b (Bracciali et al., 2016) for ZFT, samples C (Lang et al., 2016) and S5 (Gemignani et al., 2018) for MAr, and sample LI10-03b (Bracciali et al., 2016) for RUPb. Siji section samples are from Lang et al. (2016). For consistency, single-grain age populations for all these samples were decomposed from the raw data in exactly the same manner as for our new data. Depositional ages for the Siji section were based on the magnetostratigraphy of Lang et al. (2016) with a revised correlation to the Geomagnetic Polarity Time Scale (GPTS) as proposed by Govin et al. (2018), which resolves previous inconsistencies and provides a common age model consistent with data from Govin et al. (2018), Lang et al. (2016), and this study.

Reasons for obtaining inconsistent minimum-age peaks

Inferred minimum-age peaks were deemed internally consistent if the ages were in order with respect to thermochronometer closure temperature within a sample (i.e. ZFT age \leq MAr age \leq RUPb age, within error), and if they increased monotonically with depositional age for the same thermochronometer between samples. Minimum-age peaks that did not meet these two criteria were deemed internally inconsistent; they are indicated in Table S1 in regular (non-bold) font. Here, we will briefly outline some reasons why some of the age peaks are internally inconsistent.

The ZFT data are most strongly affected by this criterion, with 6 out of 16 ZFT minimum-age peaks classified as inconsistent. One reason for this may be the annealing

kinetics: predicted ZFT closure temperatures for zircons with zero α -damage (Rahn et al., 2004) are close to those for the MAr system using the diffusion parameters of Hames and Bowring (1994) in 250- μm mica grains (Fig. S5), so some overlap is to be expected. However, we also note that inconsistent ZFT minimum ages are generally obtained in samples with either a small total number ($\ll 100$) of grains counted (i.e., samples REM11, REM21, 5b) and/or a small number (< 20) of grains making up the minimum-age population (i.e., samples REM7, REM11, REM20, REM21), leading us to suggest that the counting statistics in these samples are insufficiently precise to accurately determine a minimum age (see Naylor et al., 2015 and Vermeesch, 2019 for detailed discussions).

The MAr and RUPb data are much less affected, with respectively only two and one sample inferred to be inconsistent. Sample REM3 yielded inconsistent results for all three thermochronometers; we previously interpreted this Upper Siwalik sample as containing a significant proportion of recycled Siwalik sediment (Govin et al., 2018). Finally, all of the samples from the Siji section (Lang et al., 2016) were inconsistent with ours according to the above criteria when using the original magnetostratigraphic correlation for that section, but became consistent when using the alternative correlation proposed in Govin et al. (2018).

Fitting lag-time trends

Trends of increasing, decreasing and constant lag times with depositional age can be associated to increasing, decreasing and steady exhumation rates through time, respectively (Bernet et al., 2001). In order to infer these trends from the data and rigorously assess whether the lag-time trends of minimum-peak ages as shown in Fig. 2 are better described by single- or multi-tier linear regressions, we use a Bayesian fitting technique originally developed for age-elevation profiles (Glotzbach et al., 2011). First, we fit a single straight line to the data (minimum peak ages as dependent variable and depositional ages as independent variable) for each thermochronometer, using least-square regression weighted according to the uncertainties in both ages (York et al., 2004). Then we fit the data by every possible combination of two- and three-tier linear segments, with each segment encompassing at least two data points. We assess the fit of each (single- or multi-tier) linear regression using the log-likelihood L :

$$\ln L = - \sum_{i=1}^n \left(\frac{\ln(2\pi)}{2} + \ln \sigma_i + 0.5 \left(\frac{o_i - p_i}{\sigma_i} \right)^2 \right) \quad (1)$$

where o_i , p_i , and σ_i are the observed and predicted age and the uncertainty, respectively, of the i^{th} sample; n is the number of samples considered. We use the Bayesian Information Criterion (*BIC*) to assess the appropriate model complexity, i.e. which of the single- or multi-tier regressions describes the data trends best:

$$BIC = -2 \ln L + k \ln(n) \quad (2)$$

where k and n are the number of free parameters and samples respectively; the fit that minimizes the *BIC* is considered the most appropriate. The resulting fits are shown in Fig. S4. For each thermochronometer, the three-tier fit provides the best description of the data (lowest *BIC* value); breakpoints for the multi-tier fits are systematically either around 0.5-2.0 Ma or around 7 Ma. For the three-tier fits, all lag-time plots are characterized by a regression slope $B \approx 1$ for samples with depositional ages between 0.5-2.0 and ~ 7 Ma, while the trend lines have slopes significantly above 1 for the segments younger and older than this (except for the ZFT data, which show a lower slope between 0.5 and 2.0 Ma). Adding further segments to the multi-tier linear fit does not improve the fit, as shown by increasing *BIC* values.

Thermal-kinematic inverse modeling

In order to provide a robust estimate of the onset time of rapid exhumation in the Namche Barwa syntaxis, as well as to assess the possibility of changing exhumation rates through time, we inverse-model the data using a 1-D version of the thermo-kinematic modeling code *Pecube* (Braun et al., 2012). The model predicts the time-evolution of thermochronometric cooling ages at the surface following an imposed exhumation history, which we compare to the minimum-peak ages observed in the detrital data. We therefore model the most rapidly exhuming part of the syntaxis (inferred to be the core of the Namche Barwa massif), implicitly assuming that the locus of most rapid exhumation has remained fixed through time. *Pecube* accounts for heat advection during exhumation and predicts thermochronometric ages using an empirical mathematical model for fission-track annealing, and analytical diffusion models for isotope-based thermochronometers (Braun et al., 2012). The 1D model neglects lateral heat transfer out of the system as well as potential temporal variations in topographic relief. The former is insignificant in the core of the massif compared to the extreme vertical component of heat transfer (Zeitler et al., 2014). Varying topographic relief is extremely hard to resolve from detrital data (Whipp et al., 2009).

Thermal and kinetic parameters used in the model are reported in Table S5. We use the annealing parameters for zero-damage zircon (Rahn et al., 2004) and the annealing equations of Galbraith and Laslett (1997) for predicting ZFT ages; the diffusion parameters of Hames and Bowring (1994) and an average grain size of 250 μm for predicting MAr ages; and the diffusion parameters of Cherniak (2000) and a grain size of 100 μm for RUPb ages. We use zero-damage zircon-annealing parameters (Rahn et al., 2004) because we expect the Namche Barwa zircons to have cooled rapidly from high temperatures and therefore to have developed very little α -damage. Grain sizes implemented for the MAr and RUPb systems correspond to the average grain sizes in our data. More recent ^{40}Ar diffusion parameters for white mica (Harrison et al., 2009) suggest significantly higher Ar retentivity in mica than predicted by the Hames and Bowring (1994) parameters. However, the frequent overlap between ZFT and MAr minimum-age peaks suggests a relatively similar closure temperature (see above), which is better captured by the Hames and Bowring (1994) diffusion kinetics. Smye et al. (2018) have shown that the experimentally determined diffusion parameters for Pb in rutile (Cherniak, 2000) are in excellent agreement with available empirical RUPb data. Figure S5 shows a schematic overview of the modeling approach and the inferred closure temperatures for the three thermochronometric systems.

We use the code in inverse mode, employing the Neighborhood-Algorithm inversion (Sambridge, 1999a; 1999b) to explore the parameter space. We run all models for 15 m.y. and explore both two-stage and three-stage exhumation scenarios. We did not test a single-stage scenario since inspection of the lag-time plots (Fig. 2; Fig. S4) shows that such a model can be discarded. Two-stage exhumation scenarios correspond to a three-parameter model; inverted parameters are the initial (slower) and final (rapid) exhumation rates, which were allowed to vary between 0 and 2 km/m.y. and between 2 and 10 km/m.y., respectively, and the onset time of rapid exhumation, allowed to vary between 0 and 15 Ma (i.e. over the entire model run time). Three-stage scenarios correspond to a five-parameter model, in which an intermediate exhumation rate, allowed to vary between 0 and 10 km/m.y., and a second acceleration time, between 0 and 5 Ma, were added, while the onset time for the intermediate phase was allowed to vary between 5 and 15 Ma (Table S6). In all models, the uncertainty in depositional ages was taken into account by varying the times at which thermochronometer ages were calculated and compared to the data randomly within the depositional age span for each sample (Table S1).

Pecube inversion using the Neighborhood Algorithm is a two-stage procedure (Braun et al., 2012). In the “sampling” stage, the model searches the parameter space to derive optimal (best-fit) values for the exhumation rates and time(s) of change. The fit to the data is determined by the χ^2 statistic, which is the third term in the summation of Eq. (1). An ensemble of 10,000 forward models was explored during this stage, composed of 20 iterations of 500 models each, with subsequent iterations resampling the parameter space defined by the best-fit 90% models of the previous iteration to avoid convergence in local minima. In the “appraisal” stage, the model ensemble is resampled to derive estimates of the precision with which the different parameters are resolved. This phase produces a posterior probability-density function (pdf) of the parameter values, from which a “most likely” value and its standard deviation can be inferred. Finally, we use the log-likelihood and BIC as above to assess the appropriate model complexity.

Different inversions were run, corresponding to different sets of input data and (two- or three-stage) exhumation scenarios; the results are reported in Table S6. Initial inversions (inversions 1, 2; Table S6; Figure S6) took into account all the data and solved for a two-stage scenario. These predicted a late onset time (~ 1.7 Ma) of rapid exhumation, with exhumation rates ~ 2 km/m.y. before that and very rapid rates (~ 10 km/m.y.) after (NB, here we will quote the best-fit parameter values for brevity; the most-likely parameter values and their standard deviation are given in Table S6). However, these inversions were deemed unsatisfactory, due to the poor fit to the data, the relatively low precision of the inverted parameters and the highly asymmetric posterior pdf’s. In order to assess to what degree this result was controlled by the very low errors on the minimum-peak ages for the modern samples (which contained significantly more grains than for the sedimentary samples), we reran the inversion for the same data set but increasing the error on the modern-day minimum ages by a factor 10 to make it comparable to the other errors (inversion 2). The results did not change (Table S6).

Subsequent inversions used only the internally consistent data, excluding (inversion 3) or including (inversion 4) the data from the Siji section downstream (Lang et al., 2016). In stark contrast to the previous inversions, these predicted early onset times of rapid exhumation (~ 7.8 Ma), with exhumation rates ~ 1 km/m.y. before that and rates ~ 4.5 - 6.5 km/m.y. after (Table S6, Figure S7). The only difference between inversions 3 and 4 was the higher final exhumation rate when including the Siji data (inversion 4). These results are comparable with (but better resolved than) previous modeling by Lang et al. (2016), who

modeled the Siji data alone and suggested a 5-10-fold increase in exhumation rates at 5-7 Ma and final rates of 5-10 km/m.y. Inversions 3 and 4 provided significantly better fits to the overall data and symmetric posterior pdf's, but showed no improvement in parameter resolution.

Given the above results and the optimal three-tier fits to the lag-time trends, we tested a three-stage exhumation scenario in the following inversions. Inversion 5, which used the same input data as inversion 3, predicted an early onset time (~ 7.7 Ma), a late second acceleration (~ 0.6 Ma) and best-fit initial, intermediate, and final exhumation rates of ~ 1.0 , ~ 4.2 and ~ 6.8 km/m.y. respectively, with a significantly better fit to the data (Table S6). This inversion thus provides an indication of a late further increase in exhumation rates; however, the most-likely intermediate and final rates overlap within error (5.2 ± 2.4 versus 5.3 ± 1.9 km/m.y.) and the timing of the acceleration is not well constrained (2.5 ± 1.7 Ma). When reverting to the real errors on the modern data (inversion 6), the predicted acceleration time becomes significantly better constrained (1.3 ± 0.8 Ma) and the predicted final exhumation rate significantly higher (8.6 ± 1.0 km/m.y.). This is our preferred inversion shown in Fig. 3 of the main paper, and it fits the data significantly better than a two-stage exhumation scenario fit to the same data set (inversion 7; cf. Table S6).

Justification for interpreting rutile U-Pb ages as cooling ages

In our analysis and modeling, we treat all minimum-peak ages as cooling ages. Whereas this appears reasonable for the ZFT and MAr systems, it requires justification for the RUPb system, as metamorphic rutile crystallization has been documented at temperatures as low as ~ 430 °C, i.e. well below the inferred closure temperatures (Fig. S5), by both empirical and theoretical petrology studies (Zack et al., 2004; Yakymchuk et al., 2017), depending on pressure and bulk-rock composition.

Petrological data from the Namche Barwa massif (Palin et al., 2015; Zhang et al., 2018), the indubitable source of the young rutiles in our study, suggest formation of rutile during the prograde path and at or just below peak-metamorphic conditions (Fig. S8). Rocks from the core of the Namche Barwa massif exhibit metamorphic assemblages that equilibrated at temperatures no less than ~ 650 °C (see compilation by Palin et al., 2015). Superimposed on the rutile stability field for an average metapelite recently reported by Yakymchuk et al. (2017), these P - T - t paths imply rapid subsequent cooling to the surface, and preservation of rutile formed at peak-metamorphic conditions, without significant

retrograde-path equilibration (Fig. S8A). The choice of an average metapelite composition was motivated by the desire to illustrate a “worst-case scenario” for Namche-Barwa bulk-rock composition, using this reactive rock type. In fact, limited petrological data indicate that felsic and mafic gneisses, mafic granulites, and migmatites, likely sourced from Indian plate lower crust, dominate Namche-Barwa bulk-rock compositions (see compilation by Booth et al., 2008). Comparison of the rutile stability field for, and mineral assemblages in, a mafic granulite from the core of the syntaxis (Zhang et al., 2018) also precludes retrograde-path equilibration in the rutile stability field (Fig. S8B), likewise indicating that rutile U-Pb ages from syntaxial rocks should record cooling, as opposed to sub-closure-temperature crystal growth.

The mylonite zone delimiting Namche Barwa to the northwest may be an exception in that it shows equilibration at ~400-500 °C (Palin et al., 2015), i.e., conditions amenable to crystalizing rutile at temperatures below the inferred closure temperature for Pb in rutile (Fig. S8A). However, this potential source is spatially very limited.

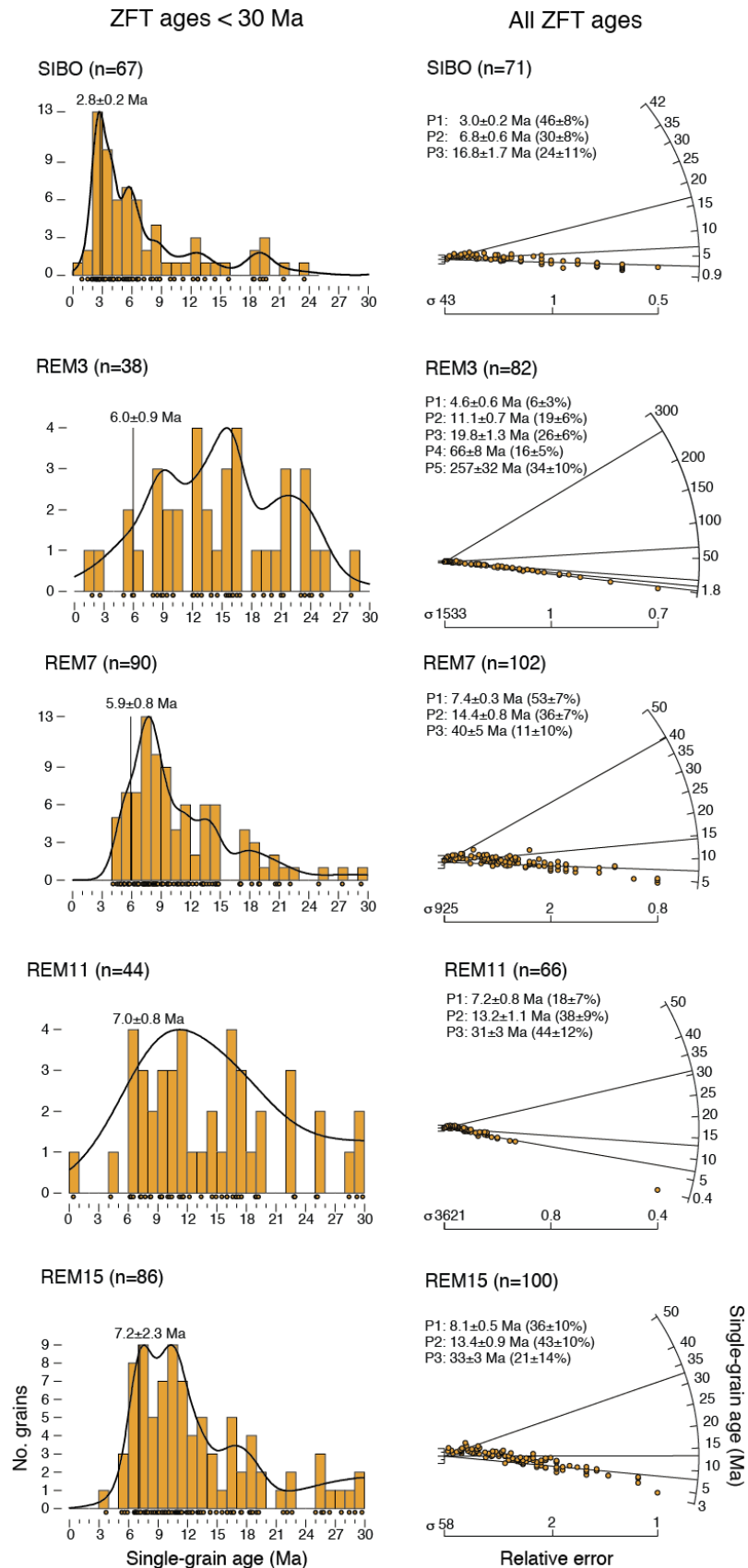


Figure S1. Zircon fission-track (ZFT) data. Left panels show histograms and kernel density estimators (KDE; Vermeesch, 2012) for single-grain ages <30 Ma; minimum peak age is indicated by vertical line; n = number of grain ages <30 Ma. Right panels show radial plots for all the data (n = total number of grains analyzed) and automatic decomposition into peak ages. Age peaks and their relative weights are indicated.

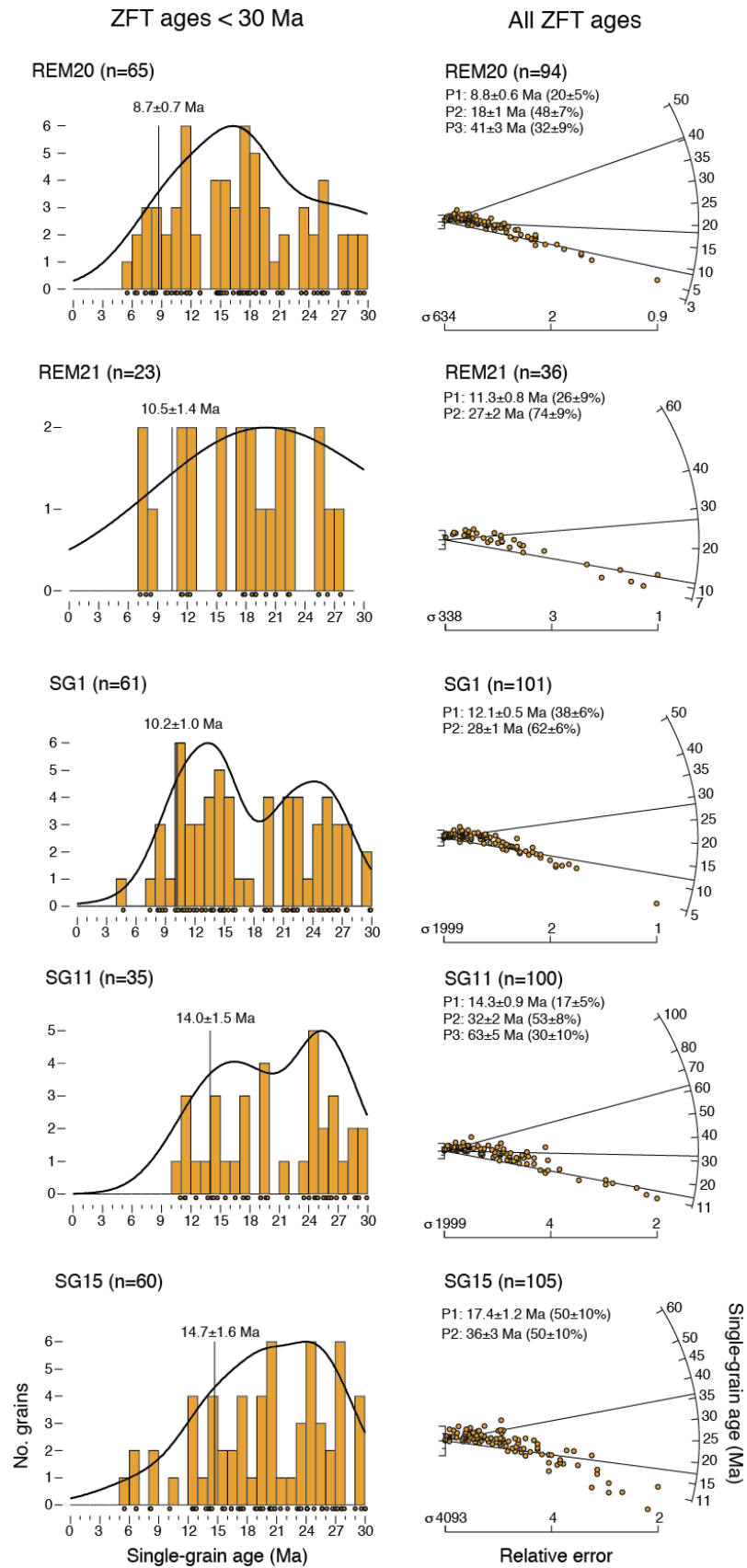


Figure S1 (continued).

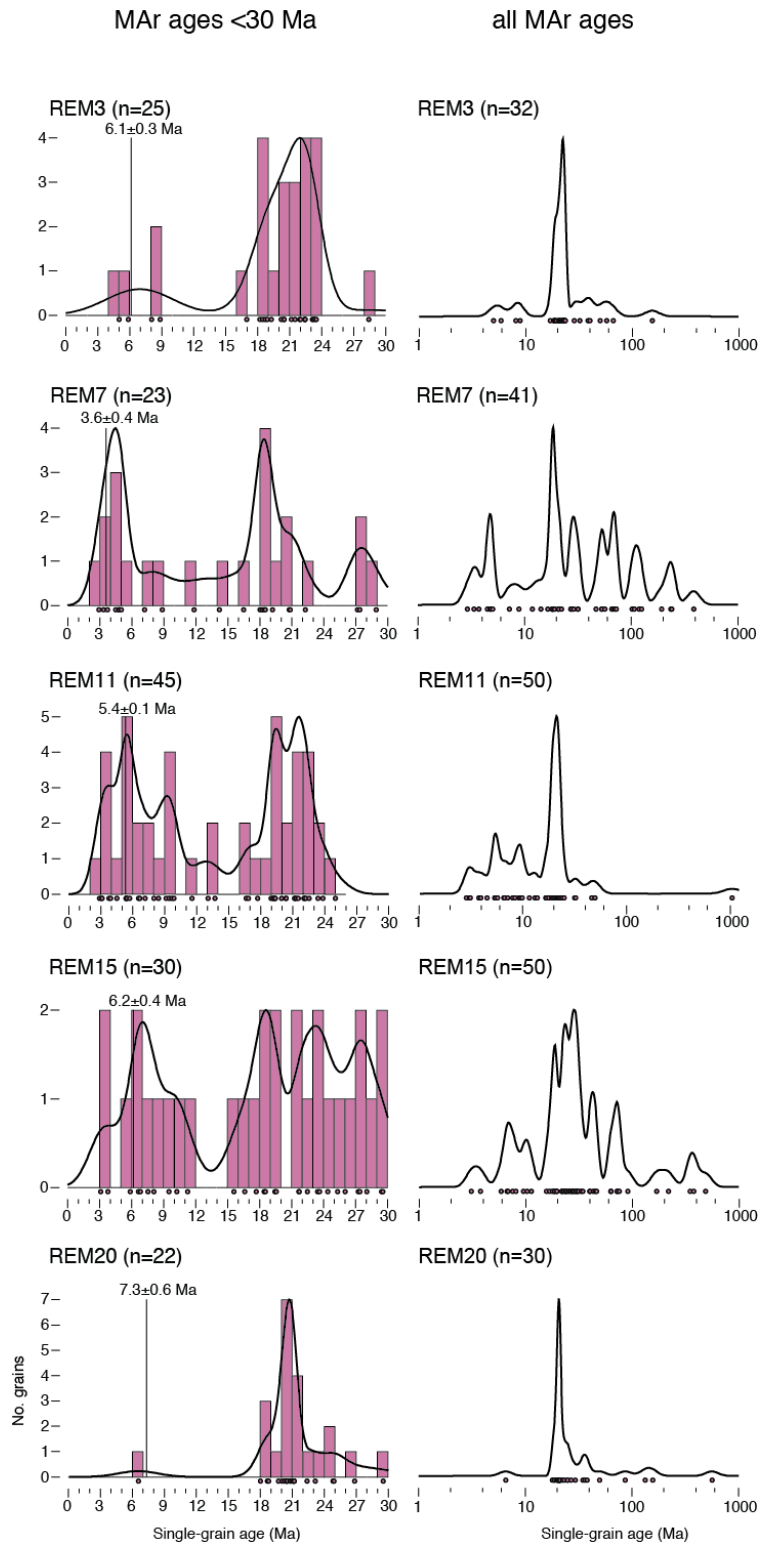


Figure S2. White-mica $^{40}\text{Ar}/^{39}\text{Ar}$ (MAr) data. Left panels show histograms and kernel density estimators (KDE; Vermeesch, 2012) for single-grain ages <30 Ma; minimum peak age is indicated by vertical line; n = number of grain ages <30 Ma. Right panels show KDE with a logarithmic time scale for all the data (n = total number of accepted grain ages).

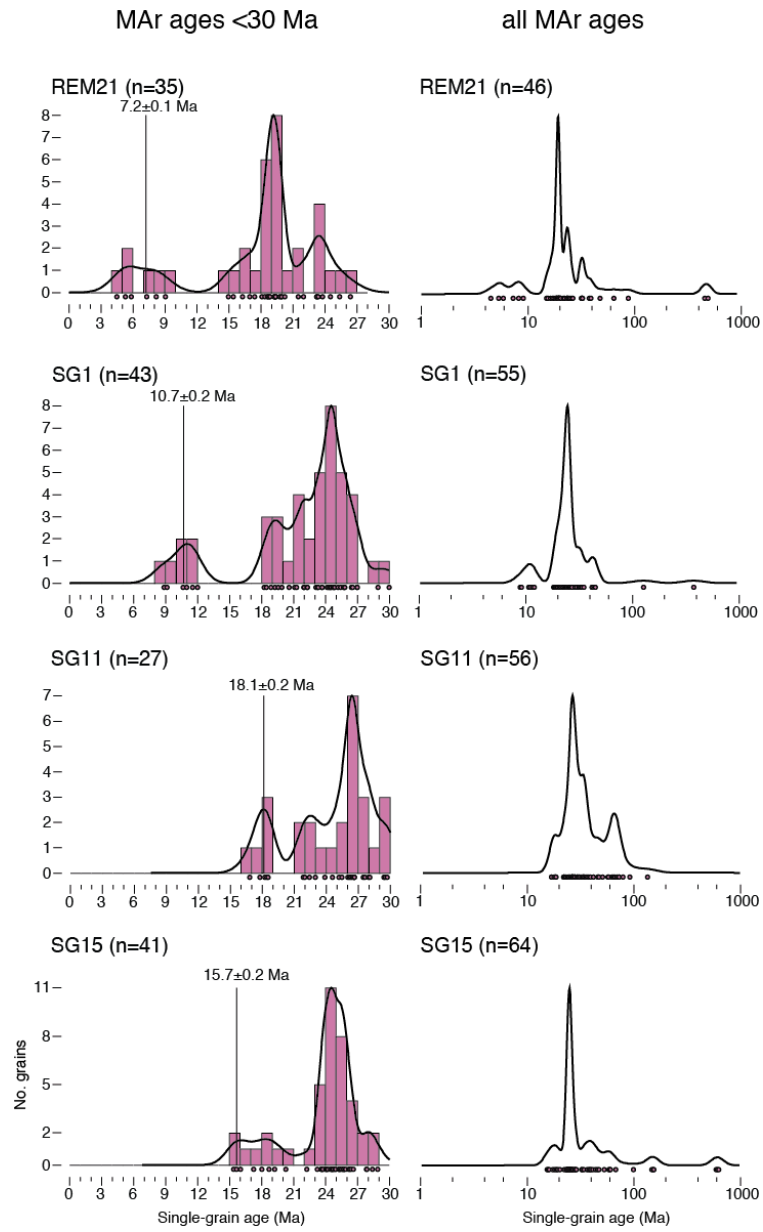


Figure S2 (continued).

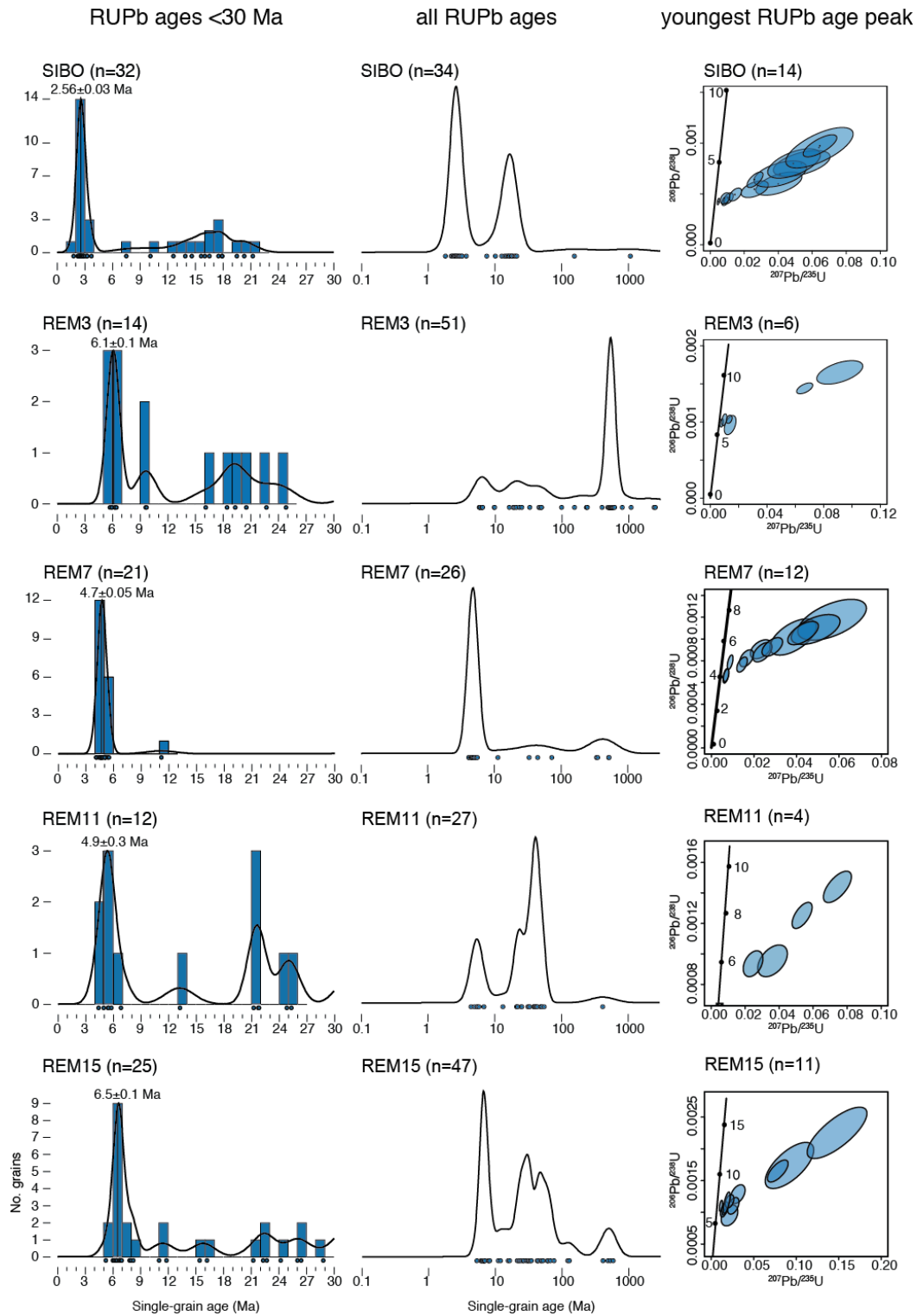


Figure S3. Rutile U-Pb (RUPb) data. Left panels show histograms and kernel density estimators (KDE; Vermeesch, 2012) for single-grain ages <30 Ma (samples SIBO-REM15) or <50 Ma (samples REM20-SG15); minimum peak age is indicated; n = number of grains included in the plot. Middle panels show KDE with a logarithmic time scale for all the data (n = total number of accepted grain ages). Right panels show Concordia (Wetherill) plots for the group of data defining the minimum peak age (n = number of grains included in the plot). Concordia plots were created using IsoplotR (Vermeesch, 2018).

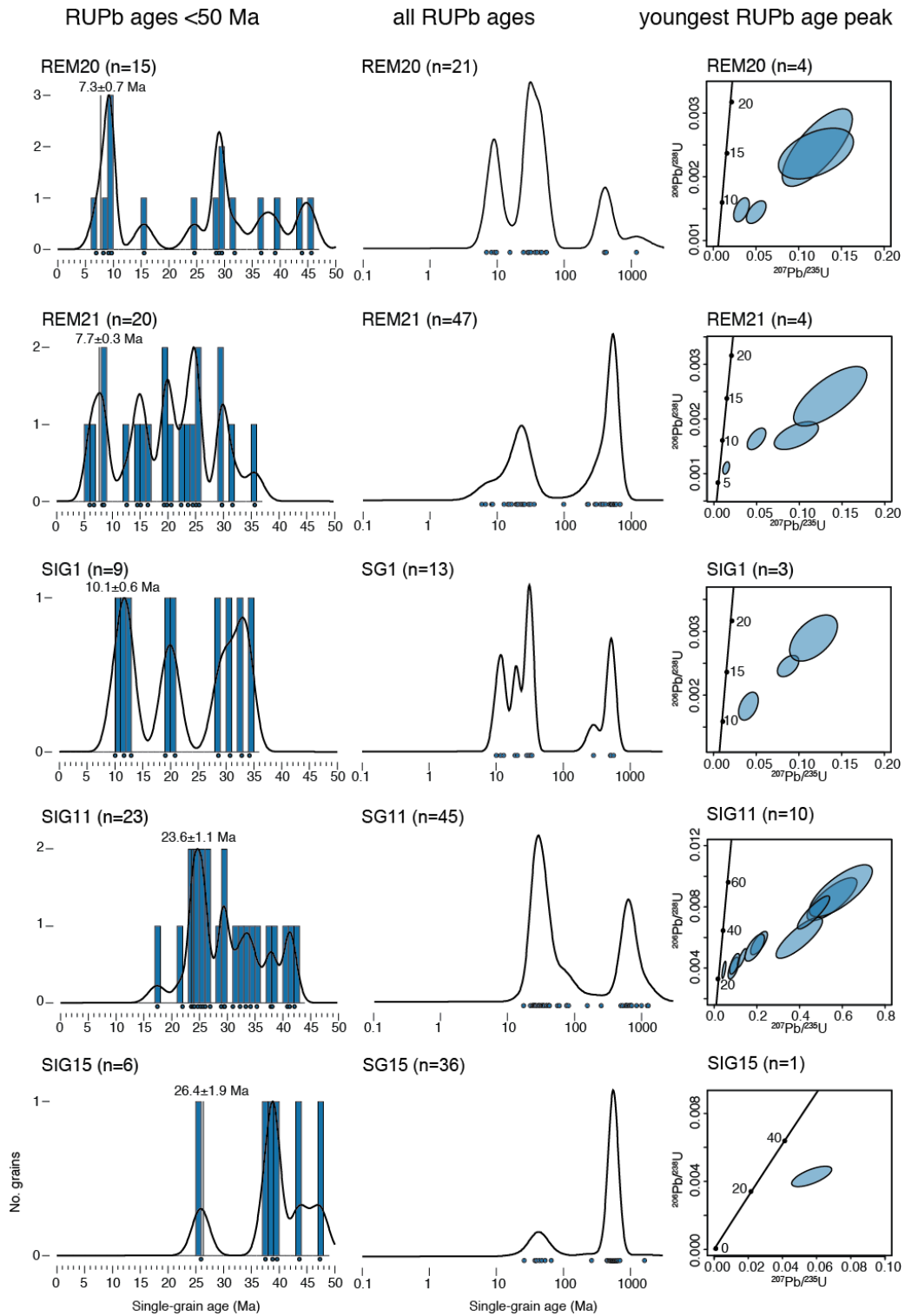


Figure S3 (continued).

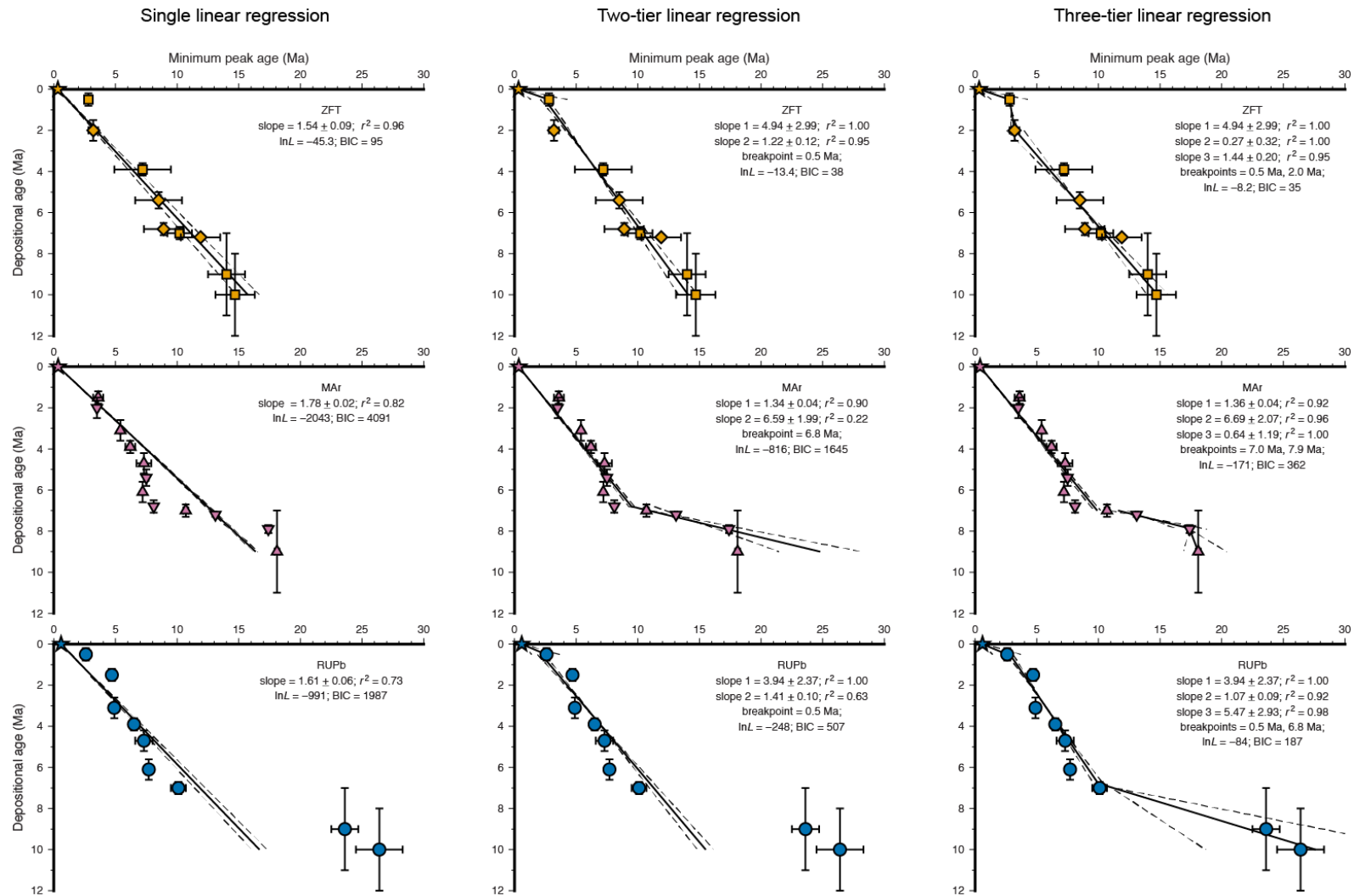


Figure S4. Least-square fits of single, two-tier and three-tier linear segments to the lag-time data. Slope of regression lines, correlation coefficient (r^2), breakpoints, log likelihood ($\ln L$) and Bayesian Information Criterion (BIC) are indicated for each fit. Colors and symbols are as in Fig. 2; note that only internally consistent data have been fitted.

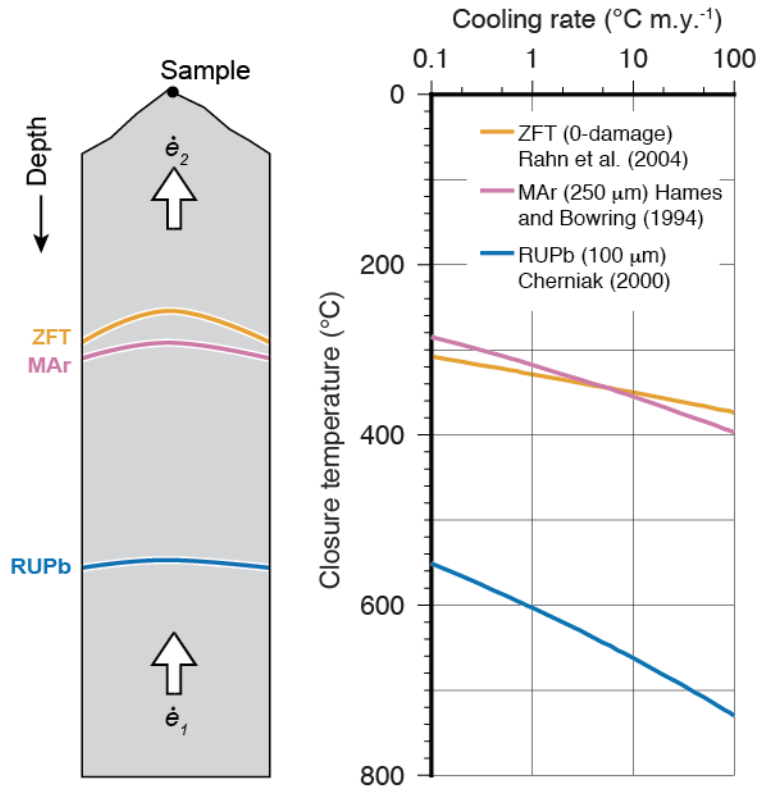


Figure S5. Modeling approach and thermochronometric systems. The 1D thermo-kinematic model predicts the time-evolution of thermochronologic cooling ages at the surface following an imposed exhumation history (\dot{e}_1 and \dot{e}_2 indicate initial and final exhumation rates, respectively). Right panel shows closure temperatures (Reiners and Brandon, 2006) for the three thermochronometric systems using the kinetic parameters in Table S5, as a function of cooling rate. Note that the model does not use these closure temperatures but rather forward-models the ages directly using the predicted thermal history and the adopted annealing / diffusion models.

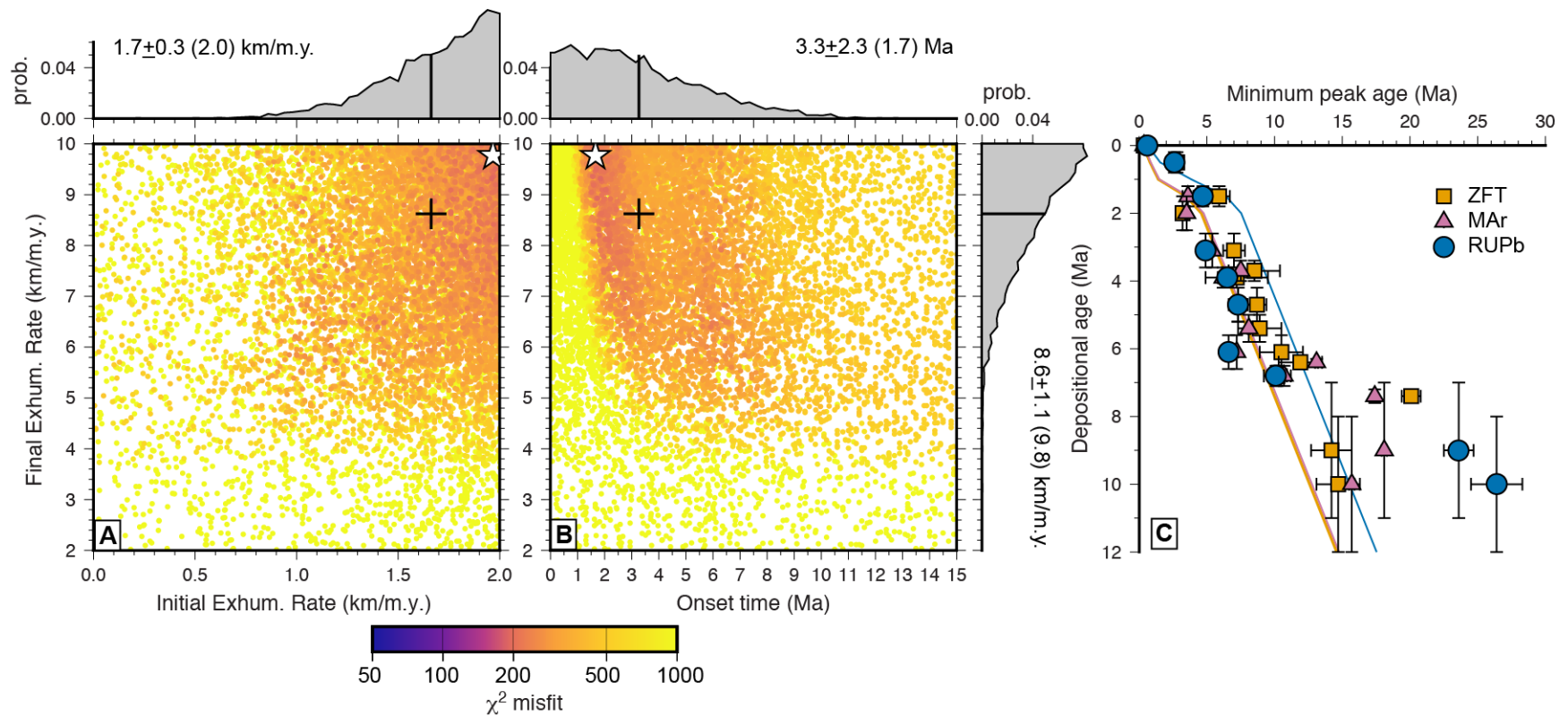


Figure S6. Result of two-stage thermal-kinematic model inversion using all data (inversion 2). A, B: individual forward-model results (dots colored according to misfit) and posterior probability-density functions (pdf's) of the parameter values; for (A) initial exhumation rate versus final exhumation rate; (B) onset time versus final exhumation rate. Crosses in scatterplots and thick lines in pdf's indicate most likely values of parameters, indicated next to pdf with its 1σ uncertainty; stars indicate absolute best-fit model parameters (indicated in parentheses next to pdf's). C: fit of the best-fit model (colored lines; orange = ZFT, purple = MAr; blue = RUPb) to the data (colored symbols with error bars).

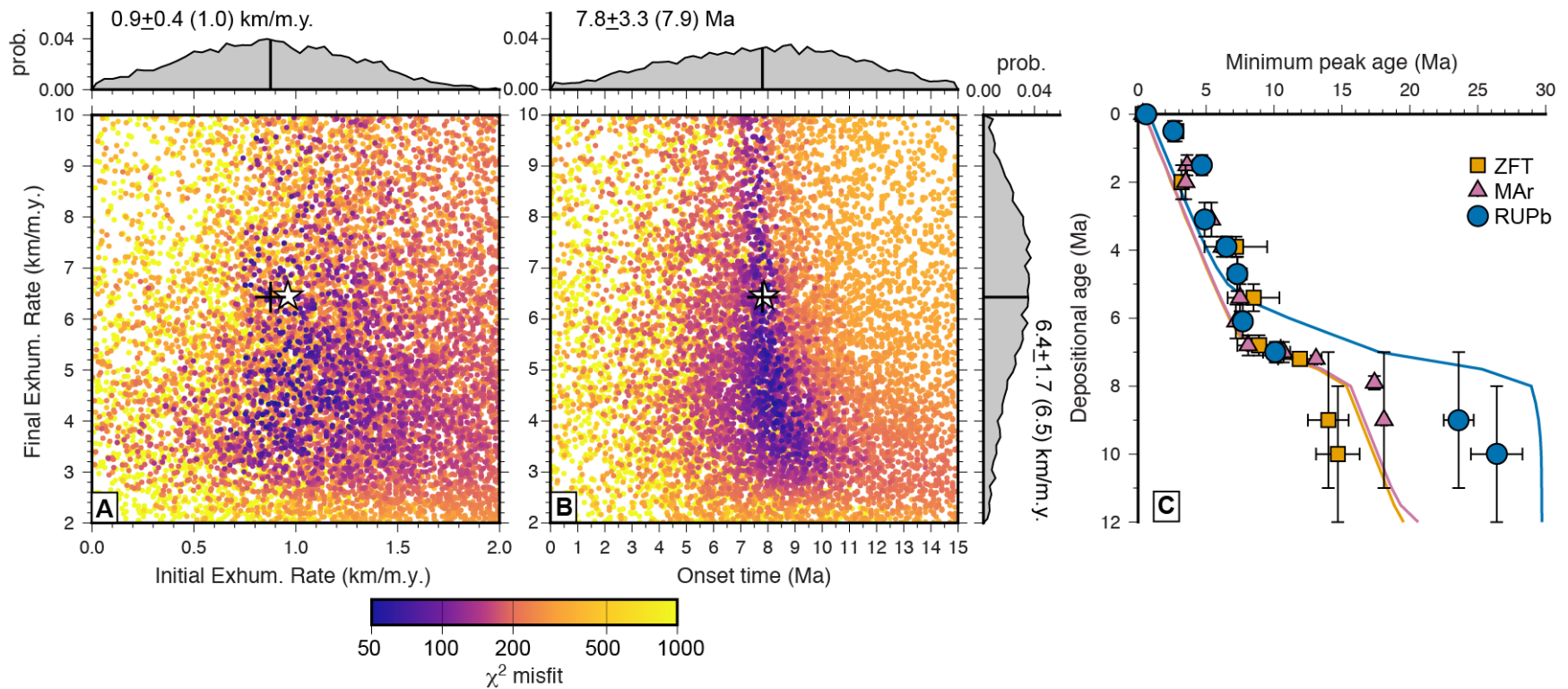


Figure S7. Result of two-stage thermal-kinematic model inversion using internally consistent data (inversion 4). A, B: individual forward-model results (dots colored according to misfit) and posterior probability-density functions (pdf's) of the parameter values; for (A) initial exhumation rate versus final exhumation rate; (B) onset time versus final exhumation rate. Crosses in scatterplots and thick lines in pdf's indicate most likely values of parameters, indicated next to pdf with its 1σ uncertainty; stars indicate absolute best-fit model parameters (indicated in parentheses next to pdf's). C: the fit of the best-fit model (colored lines; orange = ZFT, purple = MAr; blue = RUPb) to the data (colored symbols with error bars).

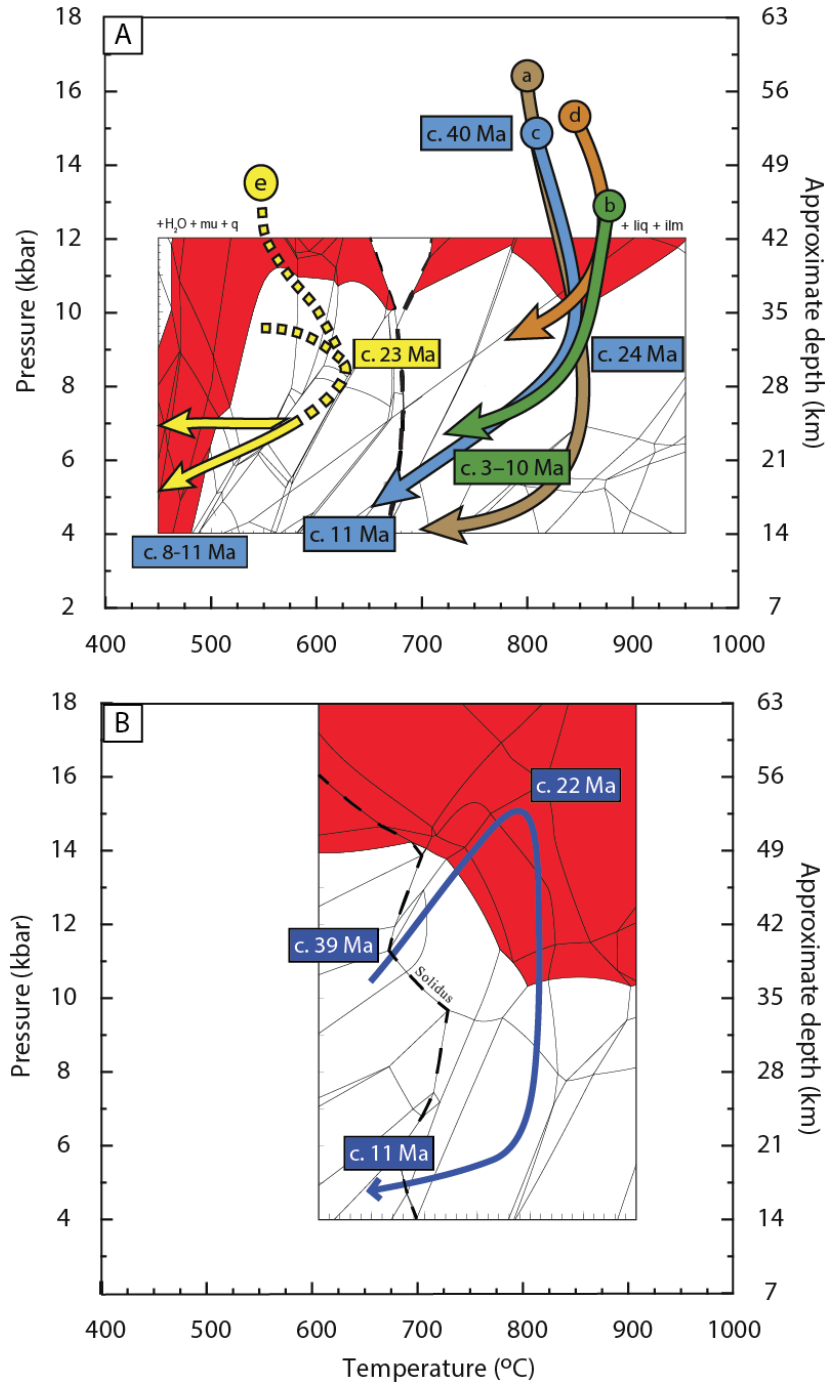


Figure S8. Metamorphic Pressure-Temperature-time (P - T - t) paths from the Namche Barwa massif. A: P - T - t paths for granulite-facies metamorphic units from the core of the massif (a-d) and from the mylonite zone bordering it to the northwest (e), modified from Palin et al. (2015), overlain on petrogenetic grid for average metapelite (Yakymchuk et al., 2017). B: P - T - t path and petrogenetic grid for a mafic granulite from the core of the massif, modified from Zhang et al. (2018), from which a 1.4-Ma rutile U-Pb age was obtained (Bracciali et al., 2016; cf. Fig. 1). Stability fields for rutile crystallization are shown in red in both (A) and (B).

Tables S2-S4 (separate files).

Table S2: Zircon fission-track (ZFT) single-grain age data. N_s and N_i are the number of spontaneous and induced tracks, respectively; ρ_s , ρ_i and ρ_d are the spontaneous, induced, and dosimeter track densities. Uncertainty on the age is given both as the lower and upper limits of the 95% Confidence Interval (C.I.) and as 2σ . Ages were determined by GG, using a ζ -factor of 105.8 ± 3.7 .

Table S3: Mica $^{40}\text{Ar}/^{39}\text{Ar}$ (MAr) single-grain age data. Abundances of the five measured Ar isotopes are indicated, from which the $^{40}\text{Ar}/^{39}\text{Ar}$ ratio and the age is calculated using the J-calibration approach. Final column (“screen”) indicates whether results were accepted or rejected and based on which criterion: (1) Analysis failed; (2) Age >20 Ma, uncertainty >20%; (3) 5 Ma < Age < 20 Ma; uncertainty >50%; (4) Age < 5 Ma; $^{39}\text{Ar V} < 0.5$; (5) Age < 5 Ma; uncertainty > 100%; (6) age accepted.

Table S4: Rutile U-Pb (RUPb) single-grain age data. Abundances of U, Th, and Pb isotopes are indicated, together with relevant ratios and calculated ages. Regressed ages, derived by regressing data points through a fixed common-Pb composition of 0.844 ± 0.008 on Tera-Wasserburg plots (Bracciali et al., 2013) are used in the analysis. Final column (“screen”) indicates whether results were accepted or rejected and based on which criterion: (1) Analysis failed; (2) $^{207}\text{Pb}/^{206}\text{Pb} > 0.5$; (3) $^{206}\text{Pb} < 100$ counts; (4) Common-Pb corrected age accepted.

Thermal parameters				
Crustal thickness	50 km			
Initial geothermal gradient	30 °C/km			
Heat production	0 $\mu\text{W}/\text{m}^3$			
Thermal diffusivity	30 $\text{km}^2/\text{m.y.}$			
Age-prediction model parameters				
System	Parameters			Reference
Zircon fission-track	$a = -11.57$	$b = 2.755 \times 10^{-4}$	$c = 1.075 \times 10^{-2}$	Rahn et al. (2004)
White-mica $^{40}\text{Ar}/^{39}\text{Ar}$	$E_a = 180 \text{ kJ/mol}$	$D_0 = 4.0 \times 10^{-4} \text{ cm}^2/\text{s}$	$d = 250 \text{ }\mu\text{m}$	Hames and Bowring (1994)
Rutile U-Pb	$E_a = 250 \text{ kJ/mol}$	$D_0 = 3.92 \times 10^{-6} \text{ cm}^2/\text{s}$	$d = 100 \text{ }\mu\text{m}$	Cherniak (2000)

Table S5: Model parameters. E_a , D_0 and d are the activation energy, pre-exponential factor and characteristic diffusion (grain) size for the diffusion models for MAr and RUPb, respectively, while a , b and c are empirical fit parameters to the “fanning Arrhenius” model of Galbraith and Laslett (1997) for ZFT.

Run	Initial exhum. rate (km/m.y.)		Intermed. exhum. rate (km/m.y.)		Final exhum. rate (km/m.y.)		Onset time (Ma)		Acceleration time (Ma)		# data				Fit parameters			Run characteristics
	best-fit	most likely	best-fit	most likely	best-fit	most likely	best-fit	most likely	best-fit	most likely	ZFT	Mar	RUPb	Total	χ^2	ln L	BIC	
prior	0-2	1,00 ±1,00	2-10	6,0 ±4,0	2-10	6,0 ±4,0	0-15	7,5 ±7,5	0-5	2,5 ±2,5								
1	1,86	1,59 ±0,31			9,67	8,06 ±1,46	1,70	3,10 ±2,28			15	14	10	39	173,4	-3382	6775	all data
2	1,97	1,66 ±0,29			9,77	8,62 ±1,06	1,66	3,27 ±2,34			15	14	10	39	157,3	-3074	6166	all data, larger errors on modern data
3	0,96	0,92 ±0,35			4,45	4,23 ±1,19	7,86	7,84 ±2,67			6	10	9	25	48,8	-607	1224	only consistent data, larger errors on modern data
4	0,96	0,88 ±0,40			6,45	6,43 ±1,70	7,86	7,80 ±3,31			10	13	9	32	44,5	-713	1437	consistent data; preferred correlation for Siji section
5	0,97	0,87 ±0,42	4,19	5,22 ±2,35	6,83	5,30 ±1,90	7,65	8,10 ±1,88	0,56	2,53 ±1,74	6	10	9	25	39,5	-490	996	3-phase model, consistent data, larger errors on modern data
6	0,99	0,88 ±0,38	4,22	4,03 ±2,00	9,36	8,62 ±1,03	7,83	8,17 ±1,79	1,08	1,28 ±0,78	6	10	9	25	70,9	-875	1766	3-phase model, including real errors on modern data
7	1,21	0,82 ±0,37			6,93	6,96 ±1,33	7,05	7,46 ±2,72			6	10	9	25	94,9	-1174	2365	2-phase model, including real errors on modern data

Table S6: Inversion Results. For each inversion run, best-fit (optimal) values together with Bayesian estimates of the most likely value and its uncertainty are given for the different input parameters. The line indicated with “prior” shows the prior bounds to these values. Two-phase models have three parameters: initial and final exhumation rate, and onset time (time of change from initial to final rates); three-phase models have five parameters: initial, intermediate, and final exhumation rates, onset time (time of change from initial to intermediate rates) and change time (time of change from intermediate to final rates). Fit parameters for optimal model are the χ^2 value, the log-likelihood (lnL) and the Bayesian Information Criterion (BIC).

Data Availability

All detrital thermochronology data for this study are reported in Tables S2-S4 available in this Data Repository. Data for successful analyses are also available at Geochron.org and EarthChem (Sibo-Remi-Siang sections detrital thermochronology, eastern Arunachal Pradesh Siwaliks; doi: [10.26022/IEDA/111598](https://doi.org/10.26022/IEDA/111598)). The 1D-version of the *Pecube* code used for this study is available on: <https://github.com/pvdbEEK/Pecube1D>.

Supplementary References

- Bernet, M., and Garver, J.I., 2005, Fission-track analysis of detrital zircon: Reviews in Mineralogy and Geochemistry, v. 58, p. 205–237, doi: 10.2138/rmg.2005.58.8.
- Bernet, M., Zattin, M., Garver, J.I., Brandon, M.T., and Vance, J.A., 2001, Steady-state exhumation of the European Alps: Geology, v. 29, p. 35–38, doi: 10.1130/0091-7613(2001)029<0035:SSEOTE>2.0.CO;2.
- Booth, A.L., Chamberlain, C.P., Kidd, W.S.F., and Zeitler, P.K., 2009, Constraints on the metamorphic evolution of the eastern Himalayan syntaxis from geochronologic and petrologic studies of Namche Barwa: Geological Society of America Bulletin, v. 121, p. 385–407, doi: 10.1130/B26041.1.
- Bracciali, L., Parrish, R.R., Horstwood, M.S., Condon, D.J., and Najman, Y., 2013, U-Pb LA-(MC)-ICP-MS dating of rutile: New reference materials and applications to sedimentary provenance: Chemical Geology, v. 347, p. 82–101.
- Bracciali, L., Parrish, R.R., Najman, Y., Smye, A., Carter, A., and Wijbrans, J.R., 2016, Plio-Pleistocene exhumation of the eastern Himalayan syntaxis and its domal “pop-up”: Earth Science Reviews, v. 160, p. 350–385, doi: 10.1016/j.earscirev.2016.07.010.
- Braun, J., van der Beek, P., Valla, P., Robert, X., Herman, F., Glotzbach, C., Pedersen, V., Perry, C., Simon-Labric, T., and Prigent, C., 2012, Quantifying rates of landscape evolution and

- tectonic processes by thermochronology and numerical modeling of crustal heat transport using PECUBE: *Tectonophysics*, v. 524-525, p. 1–28, doi: 10.1016/j.tecto.2011.12.035.
- Cherniak, D.J., 2000, Pb diffusion in rutile: *Contributions to Mineralogy and Petrology*, v. 139, p. 198–207, doi: 10.1007/PL00007671.
- Enkelmann, E., Ehlers, T.A., Zeitler, P.K., and Hallet, B., 2011, Denudation of the Namche Barwa antiform, eastern Himalaya: *Earth and Planetary Science Letters*, v. 307, p. 323–333, doi: 10.1016/j.epsl.2011.05.004.
- Galbraith, R.F., 2005, *Statistics for Fission Track Analysis*: Boca Raton, Chapman and Hall/CRC, 240 p.
- Galbraith, R.F., and Laslett, G.M., 1997, Statistical modelling of thermal annealing of fission tracks in zircon: *Chemical Geology*, v. 140, p. 123–135, doi: 10.1016/S0009-2541(97)00016-8.
- Gemignani, L., Kuiper, K.F., Wijbrans, J.R., Sun, X., and Santato, A., 2019, Improving the precision of single grain mica $^{40}\text{Ar}/^{39}\text{Ar}$ -dating on smaller and younger muscovite grains: Application to provenance studies: *Chemical Geology*, v. 511, p. 100–111, doi: 10.1016/j.chemgeo.2019.02.013.
- Gemignani, L., van der Beek, P.A., Braun, J., Najman, Y.M.R., Bernet, M., Garzanti, E., and Wijbrans, J.R., 2018, Downstream evolution of the thermochronologic age signal in the Brahmaputra catchment (eastern Himalaya): Implications for the detrital record of erosion: *Earth and Planetary Science Letters*, v. 499, p. 48–61, doi: 10.1016/j.epsl.2018.07.019.
- Glotzbach, C., van der Beek, P.A., and Spiegel, C., 2011, Episodic exhumation and relief growth in the Mont Blanc massif, Western Alps from numerical modelling of thermochronology data: *Earth and Planetary Science Letters*, v. 304, p. 417–430, doi:

10.1016/j.epsl.2011.02.020.

Govin, G., Najman, Y., Dupont-Nivet, G., Millar, I., van der Beek, P., Huyghe, P., O'Sullivan, P., Mark, C., and Vögeli, N., 2018, The tectonics and paleo-drainage of the easternmost Himalaya (Arunachal Pradesh, India) recorded in the Siwalik rocks of the foreland basin: *American Journal of Science*, v. 318, p. 764–798, doi: 10.2475/07.2018.02.

Hames, W.E., and Bowring, S.A., 1994, An empirical evaluation of the argon diffusion geometry in muscovite: *Earth and Planetary Science Letters*, v. 124, p. 161–169, doi: 10.1016/0012-821X(94)00079-4.

Harrison, T.M., Célérier, J., Aikman, A.B., Hermann, J., and Heizler, M.T., 2009, Diffusion of ^{40}Ar in muscovite: *Geochimica et Cosmochimica Acta*, v. 73, no. 4, p. 1039–1051, doi: 10.1016/j.gca.2008.09.038.

Horstwood, M., 2008, Data reduction strategies, uncertainty assessment and resolution of LA-(MC-) ICP-MS isotope data: *Mineralogical Association of Canada, Short Course Series*, v. 40.

Horstwood, M.S., Foster, G.L., Parrish, R.R., Noble, S.R., and Nowell, G.M., 2003, Common-Pb corrected in situ U–Pb accessory mineral geochronology by LA-MC-ICP-MS: *Journal of Analytical Atomic Spectrometry*, v. 18, p. 837–846.

Hurford, A.J., and Green, P.F., 1983, The zeta age calibration of fission-track dating: *Chemical Geology*, v. 41, p. 285–317, doi: 10.1016/S0009-2541(83)80026-6.

Koppers, A.A.P., 2002, ArArCALC—software for $^{40}\text{Ar}/^{39}\text{Ar}$ age calculations: *Computers and Geosciences*, v. 28, p. 605–619, doi: 10.1016/S0098-3004(01)00095-4.

Kuiper, K.F., Deino, A., Hilgen, F.J., Krijgsman, W., Renne, P.R., and Wijbrans, J.R., 2008, Synchronizing rock clocks of Earth history: *Science*, v. 320, p. 500–504, doi:

10.1126/science.1154339.

Lang, K.A., Huntington, K.W., Burmester, R., and Housen, B., 2016, Rapid exhumation of the eastern Himalayan syntaxis since the late Miocene: *Geological Society of America Bulletin*, v. 128, p. 1403–1422, doi: 10.1130/B31419.1.

Luvizotto, G.L., Zack, T., Meyer, H.P., Ludwig, T., Triebold, S., Kronz, A., Münker, C., Stockli, D.F., Prowatke, S., and Klemme, S., 2009, Rutile crystals as potential trace element and isotope mineral standards for microanalysis: *Chemical Geology*, v. 261, p. 346–369.

Naylor, M., Sinclair, H.D., Bernet, M., van der Beek, P., and Kirstein, L.A., 2015, Bias in detrital fission track grain-age populations: Implications for reconstructing changing erosion rates: *Earth and Planetary Science Letters*, v. 422, no. C, p. 94–104, doi: 10.1016/j.epsl.2015.04.020.

Palin, R.M., Searle, M.P., St-Onge, M.R., Waters, D.J., Roberts, N.M.W., Horstwood, M.S.A., Parrish, R.R., and Weller, O.M., 2015, Two-stage cooling history of pelitic and semi-pelitic mylonite (*sensu lato*) from the Dongjiu-Milin shear zone, northwest flank of the eastern Himalayan syntaxis: *Gondwana Research*, v. 28, p. 509–530, doi: 10.1016/j.gr.2014.07.009.

Rahn, M.K., Brandon, M.T., Batt, G.E., and Garver, J.I., 2004, A zero-damage model for fission-track annealing in zircon: *American Mineralogist*, v. 89, p. 473–484, doi: 10.2138/am-2004-0401.

Reiners, P.W., and Brandon, M.T., 2006, Using thermochronology to understand orogenic erosion: *Annual Review of Earth and Planetary Sciences*, v. 34, p. 419–466, doi: 10.1007/978-3-540-48684-8.

Sambridge, M., 1999a, Geophysical inversion with a neighbourhood algorithm—I. Searching a parameter space: *Geophysical Journal International*, v. 138, p. 479–494, doi: 10.1046/j.1365-

246X.1999.00876.x.

Sambridge, M., 1999b, Geophysical inversion with a neighbourhood algorithm—II. Appraising the ensemble: *Geophysical Journal International*, v. 138, p. 727–746, doi: 10.1046/j.1365-246x.1999.00900.x.

Smye, A.J., Marsh, J.H., Vermeesch, P., Garber, J.M., and Stockli, D.F., 2018, Applications and limitations of U-Pb thermochronology to middle and lower crustal thermal histories: *Chemical Geology*, v. 494, p. 1–18, doi: 10.1016/j.chemgeo.2018.07.003.

Stewart, R.J., Hallet, B., Zeitler, P.K., Malloy, M.A., Allen, C.M., and Trippett, D., 2008, Brahmaputra sediment flux dominated by highly localized rapid erosion from the easternmost Himalaya: *Geology*, v. 36, p. 711–39, doi: 10.1130/G24890A.1.

Vermeesch, P., 2012, On the visualisation of detrital age distributions: *Chemical Geology*, v. 312-313, p. 190–194, doi: 10.1016/j.chemgeo.2012.04.021.

Vermeesch, P., 2018, IsoplotR: A free and open toolbox for geochronology: *Geoscience Frontiers*, v. 9, p. 1479–1493, doi: 10.1016/j.gsf.2018.04.001.

Vermeesch, P., 2019, Statistics for Fission-Track Thermochronology, *in* Malusà, M.G. and Fitzgerald, P.G. eds., *Fission-Track Thermochronology and its Application to Geology*: Cham, Springer International Publishing, p. 109–122.

Whipp, D.M., Jr., Ehlers, T.A., Braun, J., and Spath, C.D., 2009, Effects of exhumation kinematics and topographic evolution on detrital thermochronometer data: *Journal of Geophysical Research*, v. 114, F04021, doi: 10.1029/2008JF001195.

Yakymchuk, C., Clark, C., and White, R.W., 2017, Phase relations, reaction sequences and petrochronology: *Reviews in Mineralogy and Geochemistry*, v. 83, p. 13–53, doi: 10.2138/rmg.2017.83.2.

- York, D., Evensen, N.M., Martínez, M.L., and De Basabe Delgado, J., 2004, Unified equations for the slope, intercept, and standard errors of the best straight line: *American Journal of Physics*, v. 72, p. 367–375, doi: 10.1119/1.1632486.
- Zack, T., Moraes, R., and Kronz, A., 2004, Temperature dependence of Zr in rutile: empirical calibration of a rutile thermometer: *Contributions to Mineralogy and Petrology*, v. 148, p. 471–488, doi: 10.1007/s00410-004-0617-8.
- Zeitler, P.K., Meltzer, A.S., Brown, L., Kidd, W.S.F., Lim, C., and Enkelmann, E., 2014, Tectonics and topographic evolution of Namche Barwa and the easternmost Lhasa block, Tibet: *Geological Society of America Special Paper*, v. 507, p. 23–58, doi: 10.1130/2014.2507(02).
- Zhang, Z., Ding, H., Dong, X., Tian, Z., Kang, D., Mu, H., Qin, S., Jiang, Y., and Li, M., 2018, High-temperature metamorphism, anataxis and tectonic evolution of a mafic granulite from the eastern Himalayan orogen: *Journal of Earth Science*, v. 29, p. 1010–1025, doi: 10.1007/s12583-018-0852-y.